COMPARING SPATIAL DISTRIBUTIONS OF SOLAR PROMINENCE MASS DERIVED FROM CORONAL ABSORPTION

Short title: prominence absorption

HOLLY GILBERT[1], GARY KILPER[1], DAVID ALEXANDER[2], & THERESE KUCERA[1]
[1] *NASA Goddard Space Flight Center, Code 670, Greenbelt, MD 20771*
[2] *Department of Physics and Astronomy, Rice University, Houston, TX 77005*

[1] Email: holly.r.gilbert@nasa.gov

transition region surrounding the whole prominence body, and the other in which each thread of the filamentary structure is surrounded by a tube-like transition region. Other studies measured the amount of absorption in coronal EUV observations due to prominence material to deduce prominence densities and prominence column densities (Kucera et al. 1998, Golub et al. 1999). Motivating the present study, Kucera et al. suggested looking at prominence absorption in several different coronal lines spanning each ionization wavelength regime (see Fig. 1) to determine the absolute abundances of neutral helium and hydrogen in prominences.

By observing how much coronal radiation is absorbed by a prominence low in the solar atmosphere in the EUV, it is possible to infer its mean column density and thence obtain a total prominence mass. Gilbert et al. (2005, 2006) previously applied such a technique to SOHO EIT 195 Å observations to infer prominence mass. This technique involves calculating prominence column mass density along the line of sight, and subsequently integrating this column mass density over the prominence area to find the total mass. It also allows the effects of both foreground and background radiation to be considered.

In the present work we extend the use of this mass-inference technique to a sample of prominences observed in at least two coronal lines. This approach, in theory, allows a direct calculation of prominence mass and helium abundance and how these properties vary spatially and temporally. Our motivation is two-fold: to obtain a He^0/H^0 abundance ratio, and to determine how the relative spatial distribution of the two species varies in prominences. The first of these relies on the theoretical expectation that the amount of absorption at each EUV wavelength is well-characterized. However, in this work we show that due to a saturation of the continuum absorption in the 625 Å and 368 Å lines (which have much higher opacity compared to 195 Å- Heinzel et al., 2001, 2003, 2008) the uncertainties in obtaining the relative abundances are too high to give meaningful estimates. This is an important finding because of its impact on future studies in this area. The comparison of the spatial distribution of helium and hydrogen presented here augments previous observational work indicating that cross-field diffusion of neutrals is an important mechanism for mass loss (Gilbert et al. 2007). Significantly different loss timescales for neutral He and H (helium drains much more rapidly than hydrogen) can impact prominence structure, and both the present and past studies suggest this mechanism is playing a role in structure and possibly dynamics.

Section 2 of this paper contains a description of the observations and §3 summarizes the method used to infer mass along with the criteria imposed in choosing prominences appropriate for this study. Section 3 also contains a discussion of the problems due to limitations of the available data and the implications for determining relative abundances. We present our results in §4, including plots of radial-like scans of prominence mass in different lines to show the spatial distribution of the different species. The last section contains a discussion summarizing the importance of the qualitative results found in this work. The Appendix provides a detailed derivation of how to obtain prominence mass and helium abundance (A1) and includes the data for all prominences studied (A2).

Our initial approach involves using the combination of two spectral lines to directly calculate total mass and helium abundance. We outline how that can be accomplished in a detailed derivation in the Appendix. Below we describe the basic approach followed by a discussion of why and how we adjusted the more detailed approach (Appendix) to allow for the effect of saturation of the continuum absorption in the EUV at 625Å and 368Å.

The first step in inferring prominence mass is to determine how much coronal radiation is being absorbed as it travels through the prominence. The observational measure of extinction of coronal radiation, which for 171 Å, 195 Å, and 368 Å radiation arises from hydrogen and helium continuum absorption and for 625 Å radiation arises from hydrogen continuum absorption, is represented by an extinction factor, α. If σ is the mean absorption cross section for radiation passing through a prominence, the extinction factor for radiation traveling in the direction $\hat{\mathbf{s}}$ over a distance ℓ is

$$\alpha = e^{-\int_0^{\ell} n\sigma\, ds} \tag{1}$$

Here, n is the total number density of all atoms and ions of H and He (note we assume He^{++} is negligible), and σ is given by

$$\sigma = f_H\left(1-x_H\right)\sigma_H + f_{He}\left(1-x_{He}\right)\sigma_{He} + f_{He}\,x_{He}\,\sigma_{He^+} \tag{2}$$

where the fractional hydrogen and helium abundances (by number) are represented by f_{H} and f_{He}, and the H and He ionization fractions by $x_{\mathrm{H}} = n_{\mathrm{H}^+}/(n_{\mathrm{H}} + n_{\mathrm{H}^+})$ and $x_{\mathrm{He}} = n_{\mathrm{He}^+}/(n_{\mathrm{He}} + n_{\mathrm{He}^+})$. σ_{H}, σ_{He}, and σ_{He^+} are the photoionization cross sections (for the particular line of interest) for H, He, and He^+, respectively. We assume that the absorbing material is composed only of hydrogen and helium, so

$$f_H + f_{He} = 1 \tag{3}$$

If σ is uniform throughout the prominence, and if we define the column density by

$$N = \int_0^{\ell} n\, ds \tag{4}$$

it follows that

$$\alpha = e^{-N\sigma} \tag{5}$$

$$-\ln \alpha = N\sigma \tag{6}$$

As described in the Appendix, applying this to a prominence visible in two spectral lines allows the determination of the helium abundance. The resulting He^0/H^0 abundance ratios obtained range from 0.23 – 0.51. These are much higher than expected, which is

details on the error analysis), the steps that greatly impact those calculations are repeated ten times to reduce statistical error. The scale height of the coronal emission is measured by finding the slope of a semi-log plot of the line emission versus the radius. To obtain the background radiation, we interpolate between points that are on either side of the prominence material. Since the amount of coronal radiation along a radial scan of the quiet Sun generally follows a symmetric logarithmic distribution that is peaked at the edge of the limb, we correct for small deviations in coronal emission by using a power law to smooth over any anomalies and provide a much better estimate of the coronal radiation around the prominence material. The code automatically interpolates the amount of coronal emission at all data pixels of the prominence between the two corrected radial scans, providing a map of the interpolated background radiation and effectively "deleting" the prominence material.

Using the interpolated image together with the real image, and accounting for the amount of radiation originating in front of the prominence (foreground radiation $= I_f$), we are able to obtain an extinction factor for each pixel, and thus infer a mass per pixel. The resulting "maps" showing the distribution of mass in the different lines allows a comparison of the relative spatial distribution of neutral helium and hydrogen.

3.3. EUV Absorption Error Analysis

Sources of error (other than the opacity issues discussed above) include those inherent in the method (a detailed description of the assumptions involved can be found in Gilbert et al. 2005). The determination of α introduces error because it involves looking at intensity measurements in a small region on the disk and just off the limb. The space between the intensity measurements on the disk and just off the limb needs to small (~6 pixels apart) and display relatively uniform properties throughout the localized region, so to mitigate the error associated with individual pixel fluctuations, we repeated the calculation ten times for each measurement using several pairs of data pixels to estimate the foreground radiation. We also performed various interpolations of the background radiation at different locations to study the variation. Trial runs showed that ten repetitions were enough to reduce this source of error by 2-3 times, but a greater number of repetitions did not continue decreasing the spread in the calculated masses.

Error was also reduced by prudent data selection; we excluded prominences near active regions and coronal holes to assure a better determination of the coronal radiation around each prominence. Instrumental effects were tested by several comparisons, and all were found to be relatively insignificant. For example, analyses of simultaneous TRACE and EIT observations (at either 171 Å or 195 Å) measured similar mass values, despite different resolution, exposure times, instrumentation, etc. There were also no changes detected between different exposure times and pixel sizes for EIT 195 Å observations, comparable prominence observations before and after loss of communication with SOHO in June 1998, and the different observing programs used for the CDS observations.

disk. In a previous study (Kilper et al. 2009) we found an increase of homogenization of filament mass composition at least one day prior to eruption, possibly due to an increase in activity before eruption.

5. DISCUSSION

The most significant result from this study is the additional observational support it provides for the idea that cross-field diffusion of neutral prominence material is an important mechanism in prominence mass dynamics and structure (Gilbert et al. 2002; 2007). By measuring how much coronal radiation is absorbed by prominences in different spectral lines, we are able to detect differences in the spatial distribution of helium relative to hydrogen. The lower portions of at least two quiescent prominences show a relative enhancement in the absorption in spectral lines where both hydrogen and helium are absorbers when compared to 625 Å (where only hydrogen is an absorber) indicating helium is slightly more concentrated in those lower regions. Note that this same distribution of helium is present in 368 Å and 171 Å (and in 195 Å, which is not pictured in figures 3 and 4), meaning that this absorption enhancement is unlikely to be a side-effect of the differences in opacity. It is to be expected that significant field-aligned flows of mass throughout a prominence would serve to constantly mix hydrogen and helium, thereby disrupting the observational signature of cross-field diffusion. For one prominence in our study in which flows were observed (2005 May 18), no signature of the H and He separating was apparent. A more detailed study focused on the relationship between the bulk flow of material along field lines and the mass distribution of helium and hydrogen would help address these issues. Such a study requires data with a temporal cadence and spatial resolution that allows us to observe the evolution of prominence flows while simultaneously being able to differentiate the relative distributions of H and He.

The total prominence mass calculations in Table 2 show a consistently lower mass in the 625 Å observations compared to the other lines. The significant difference in total mass between the 625 Å and 195 Å lines indicate the much higher opacity at 625 Å may be causing a saturation of the continuum absorption (as suggested in Heinzel et al., 2008) and thus, a potentially large underestimation of mass. While the opacity at 368 Å has not yet been modeled, it also has a large photoionization cross-section compared to 195 Å, and the significant difference between the masses calculated from those lines suggests that the opacity of prominences is also large at 368 Å, indicating that saturation may also be an issue for this line. At 171 Å the photoionization cross-section is even smaller than at 195 Å, which should mean that the opacity is low, yet the masses measured from the 171 Å observations are almost always smaller than those from 195 Å. The likely explanation is that hot prominence plasma is emitting in 171 Å (peaking at 1.0 MK) and reducing the amount of continuum absorption that is measured, leading to a lower mass estimate (previously found by Kucera et al 1998 and Engvold et al 2001). Quantitatively, the mass estimates from 195 Å (at 1.5 MK) benefit from a good combination of low opacity and negligible internal emission to provide the most accurate values of the total

APPENDIX

A1. DERIVING PROMINENCE MASS AND HELIUM ABUNDANCE

Recalling equations (1)-(6) in §3:

$$\alpha = e^{-\int_0^s n\sigma ds} \tag{1}$$

$$\sigma = f_H\left(1-x_H\right)\sigma_H + f_{He}\left(1-x_{He}\right)\sigma_{He} + f_{He}\,x_{He}\,\sigma_{He^+} \tag{2}$$

$$f_H + f_{He} = 1 \tag{3}$$

$$N = \int_0^s n\,ds \tag{4}$$

$$\alpha = e^{-N\sigma} \tag{5}$$

For convenience we define

$$\varepsilon = -\ln\alpha = N\sigma \tag{6}$$

we can utilize (2) and (6) to write ε in the form

$$\varepsilon = \varepsilon_H + \varepsilon_{He} + \varepsilon_{He^+} \tag{7}$$

where

$$\varepsilon_H = N\,f_H\left(1-x_H\right)\sigma_H \tag{8}$$

$$\varepsilon_{He} = N\,f_{He}\left(1-x_{He}\right)\sigma_{He} \tag{9}$$

$$\varepsilon_{He^+} = N\,f_{He}\,x_{He}\,\sigma_{He} \tag{10}$$

Note that although we define the quantities ε_H, ε_{He}, and ε_{He^+}, the only observed quantity is ε, so the parameters we wish to determine (such as N and f_{He}) are expressed in terms of ε (not in terms of ε_H, ε_{He}, and ε_{He^+}). Since we are assuming that absorption occurs only through ionization, there is a simplification for (7)-(10) at two of our wavelengths of interest (namely, 625 Å and 368 Å):

Dividing (18) by (17) we obtain

$$\frac{f_{He}}{f_H} = \left(\frac{\varepsilon_{368}}{\varepsilon_{625}} - \frac{\sigma_{H368}}{\sigma_{H625}} \right) \frac{\sigma_{H625}}{\sigma_{He368}} \frac{(1-x_H)}{(1-x_{He})} \tag{20}$$

Referring back to (3), it is readily shown that

$$f_H = \frac{1}{1 + f_{He}/f_H} \tag{21}$$

$$f_{He} = 1 - f_H \tag{22}$$

Finally, we can write the column mass, M, in the form

$$M = N\, m_H \left(f_H + 4\, f_{He} \right) \tag{23}$$

Looking back at (19)-(23), we see that it has been possible to write the column density, the column mass, and the hydrogen and helium fractions (by number) in terms of the two observed quantities ε_{625} and ε_{368}, the three known cross-sections σ_{H625}, σ_{H368}, and σ_{He368}, and the two unknown ionization fractions x_H and x_{He}. The total prominence mass can now be determined by summing all values of M (times a pixel area) over the whole prominence if a measurement is made for each pixel.

A2. MASS DISTRIBUTION AND SCANS OF THE REMAINING 8 PROMINENCES

(Figures 6-13. (a) shows the mass distribution and (b) shows the scan for each case)

FIGURE CAPTIONS

FIG. 1— average photoionization cross-section per atom/ion in a prominence with an assumed composition (45% H^0, 45% H^+, 9% He^0, and 1% He^+). In this plot, the contributions to the total photoionization cross-section are separated by the absorbing species: those due to H^0 (below the blue line), He^0 (between the red and blue lines), and He^+ (between the black and red lines) start at 912Å, 504 Å, and 228 Å, respectively (Kilper, 2009 PhD thesis; Keady & Kilcrease, 2000)

FIG. 2 — example showing the original images in CDS Mg IX and Mg X containing the prominence, the interpolated background image, and the resulting mass maps

FIG. 3 — 1996 July 31 scans in 625 Å (top left), 368 Å (top middle), and 171 Å (top right) mass maps plotted to demonstrate qualitative spatial differences in mass concentrations in the three lines. Note the differences in the scale in the 171 Å plot (right) with respect to the others. This is because the measured masses are significantly larger in 171 Å (see discussion in section 3.1). *In figures 3- 13, the solid lines in the plots show the 625 Å scans, the dashed lines show the 368 Å scans, and the dotted lines show either the 171 Å or 195 Å scans.*

FIG. 4 — 1999 Oct. 12 scans in 625 Å (top left), 368 Å (top middle), and 171 Å (top right) mass maps plotted to demonstrate qualitative spatial differences in mass concentrations in the three lines in a prominence located at position angle 310°. Note the differences in the scale in the 171 Å plot (right) with respect to the others. This is because the measured masses are significantly larger in 171 Å (see discussion above).

FIG. 5 — 2005 May 18 scans in mass maps plotted to demonstrate spatial differences in mass concentrations in two lines in a prominence located at position angle 297°: 195 Å (top left) and 625 Å (top center), 171 Å (middle left) and 625 Å (middle center), and 171 Å (bottom left) and 625 Å (bottom center). The plots in the right column show the relative distributions. Note the differences in the scale in the 171 Å and 195 Å plots with respect to 625 Å. This is because the measured masses are significantly larger in 171 Å and 195 Å than 625 Å (see discussion above).

FIGS. 6-13 — Images, interpolated backgrounds, mass maps, and scans of the mass maps for the remaining 8 prominences studied (the 1996 July 31 prominence is presented in the main text of the paper)

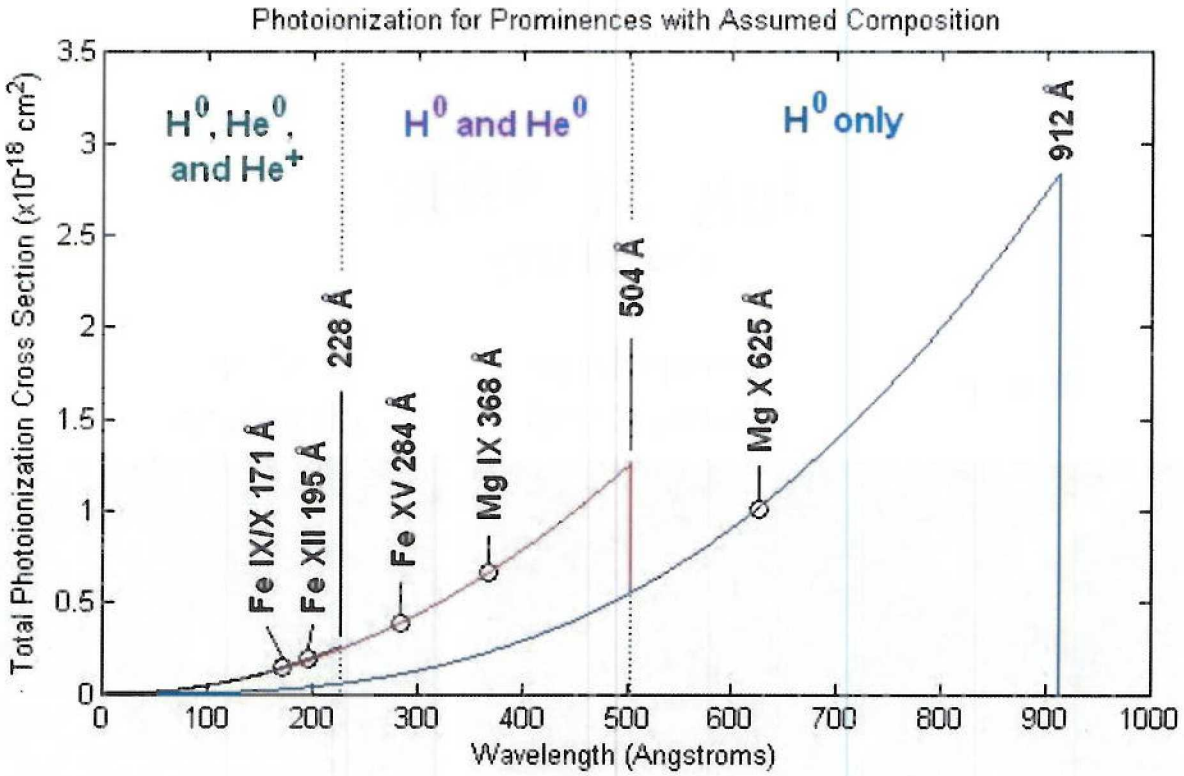
Photoionization for Prominences with Assumed Composition
Total Photoionization Cross Section (x10^-18 cm^2)
Wavelength (Angstroms)
H^0, He^0, and He^+
H^0 and He^0
H^0 only
Fe IX/X 171 Å
Fe XII 195 Å
228 Å
Fe XV 284 Å
Mg IX 368 Å
504 Å
Mg X 625 Å
912 Å
0
0.5
1
1.5
2
2.5
3
3.5
0
100
200
300
400
500
600
700
800
900
1000


SOHO/CDS 625 Å 1996
July 31, 10:58 UT


SOHO/CDS 368 Å 1996
July 31, 10:58 UT


SOHO/EIT 171 Å 1996
July 31, 07:31 UT

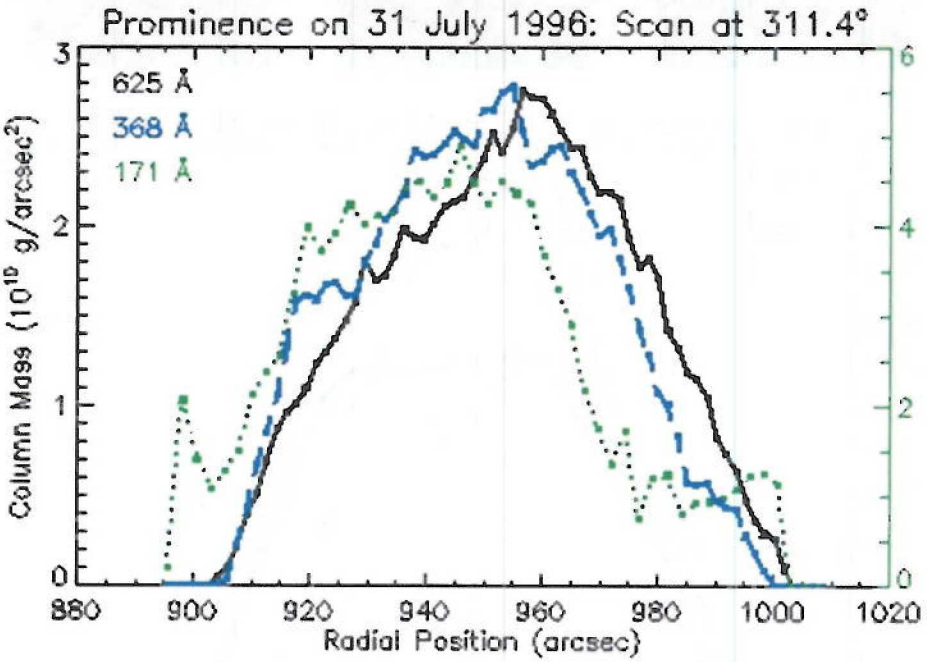
Prominence on 31 July 1996: Scan at 311.4°
625 Å
368 Å
171 Å
Column Mass (10^{19} g/arcsec^2)
Radial Position (arcsec)
0
1
2
3
4
6
880
900
920
940
960
980
1000
1020

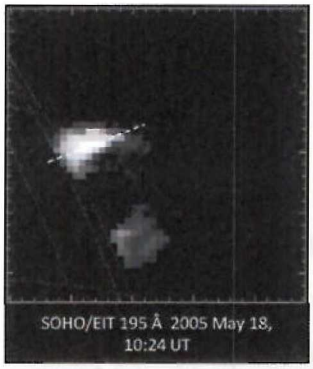

SOHO/EIT 195 Å 2005 May 18, 10:24 UT

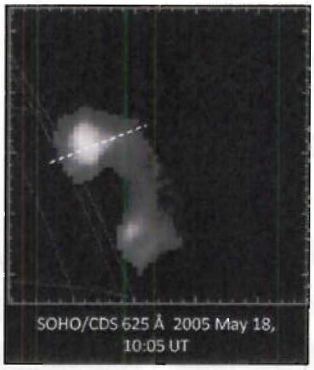

SOHO/CDS 625 Å 2005 May 18, 10:05 UT

SOHO/EIT 171 Å 2005 May 18, 19:00 UT

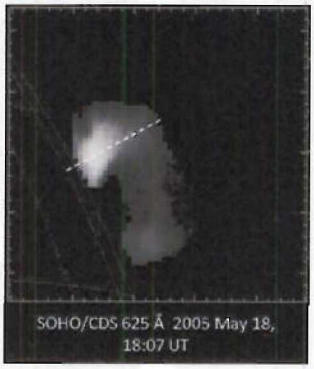

SOHO/CDS 625 Å 2005 May 18, 18:07 UT

SOHO/EIT 171 Å 2005 May 19, 01:00 UT

SOHO/CDS 625 Å 2005 May 18, 22:30 UT

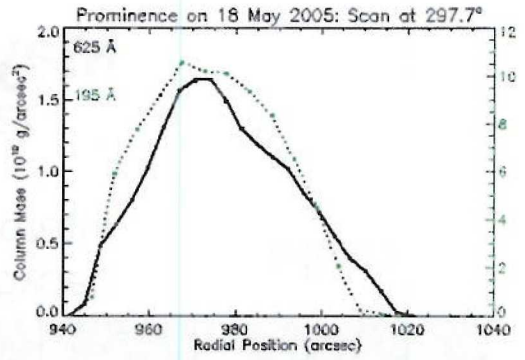

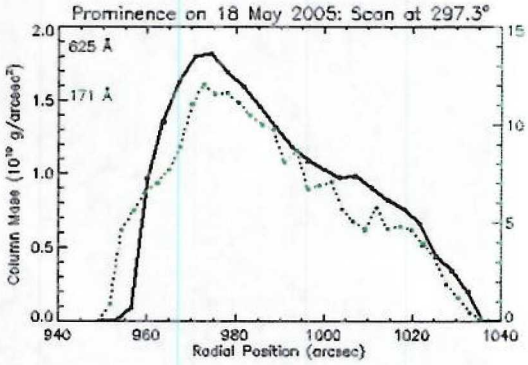

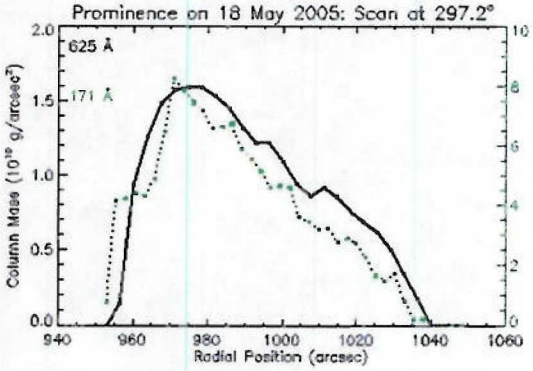

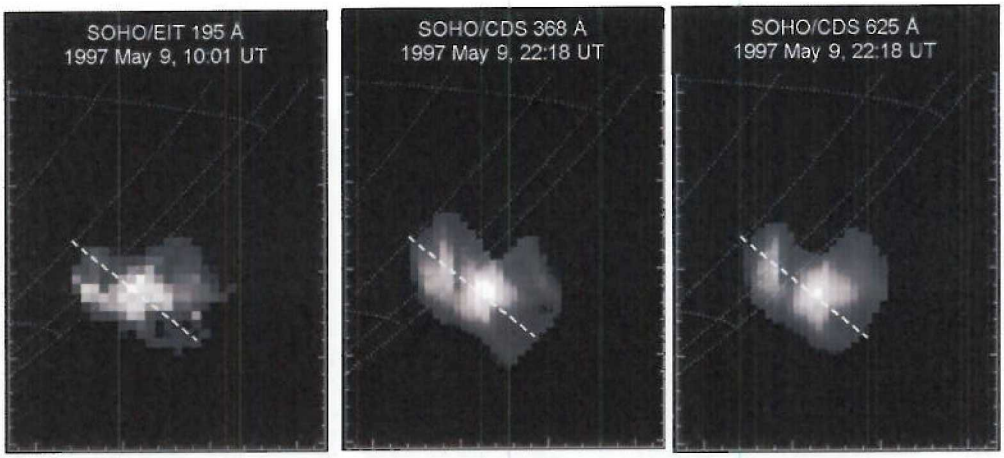
SOHO/EIT 195 Å
1997 May 9, 10:01 UT
SOHO/CDS 368 Å
1997 May 9, 22:18 UT
SOHO/CDS 625 Å
1997 May 9, 22:18 UT

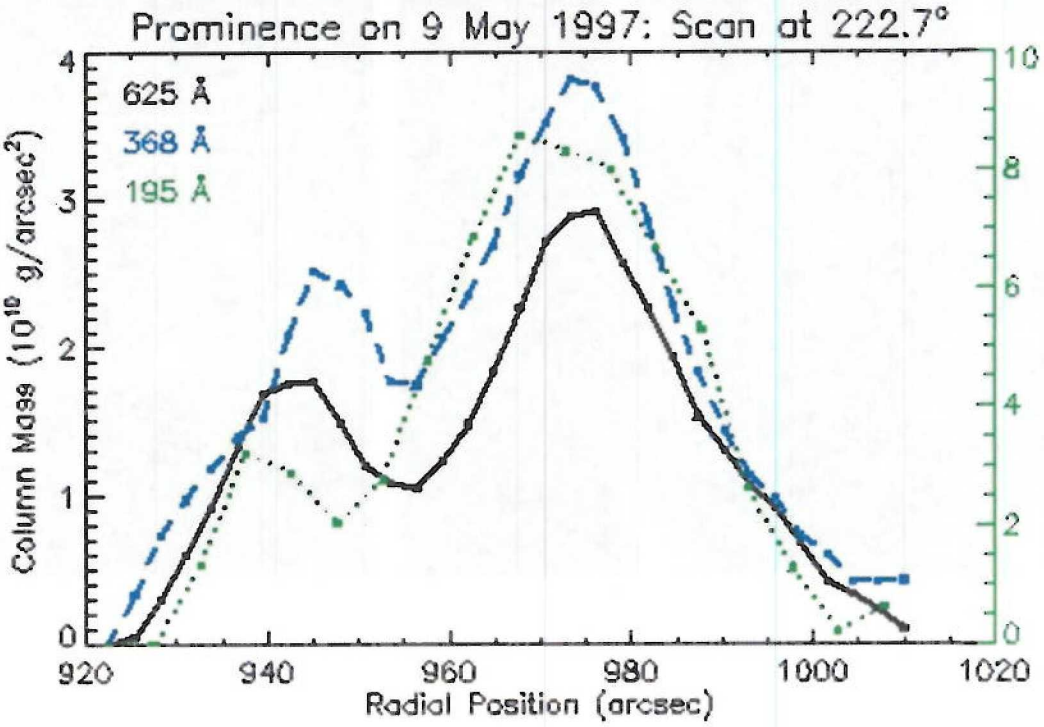
Prominence on 9 May 1997: Scan at 222.7°
625 Å
368 Å
195 Å
Column Mass (10^{19} g/arcsec^2)
Radial Position (arcsec)
0
1
2
3
4
0
2
4
6
8
10
920
940
960
980
1000
1020

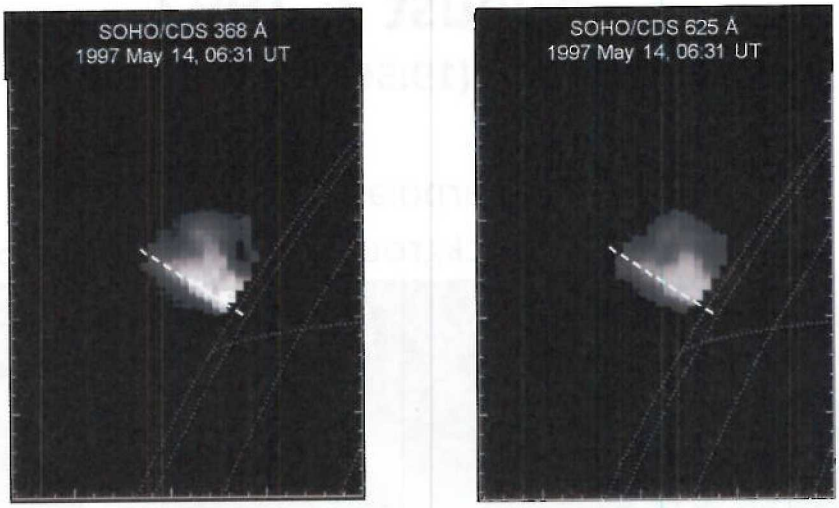
SOHO/CDS 368 Å
1997 May 14, 06:31 UT
SOHO/CDS 625 Å
1997 May 14, 06:31 UT

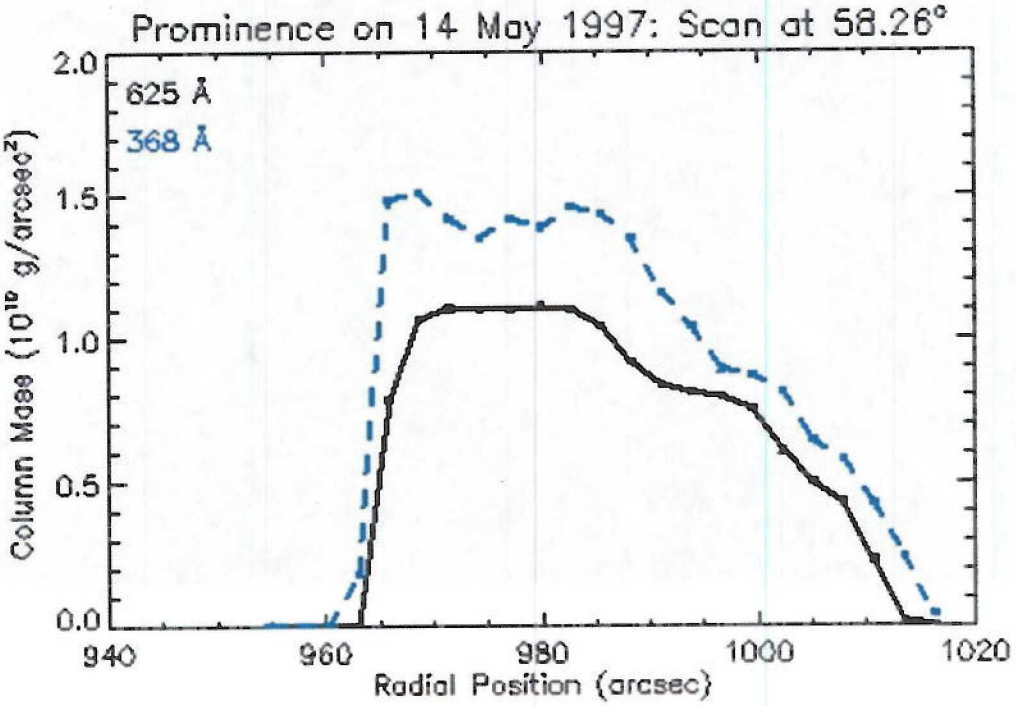
Prominence on 14 May 1997: Scan at 58.26°
625 Å
368 Å
Column Mass (10^{19} g/arcsec^2)
2.0
1.5
1.0
0.5
0.0
940
960
980
1000
1020
Radial Position (arcsec)

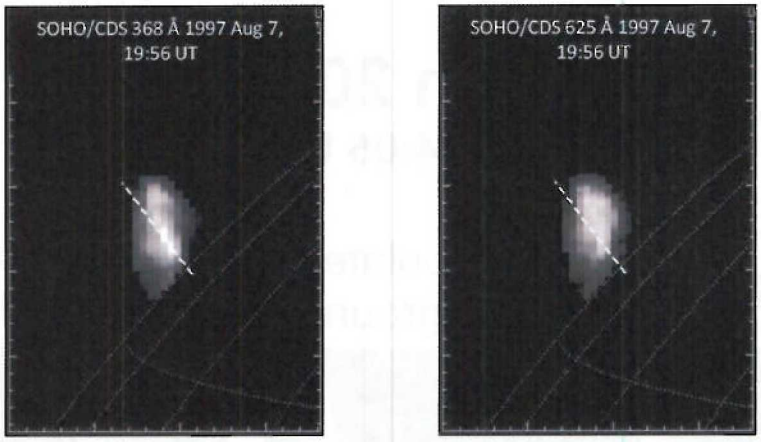
SOHO/CDS 368 Å 1997 Aug 7,
19:56 UT
SOHO/CDS 625 Å 1997 Aug 7,
19:56 UT

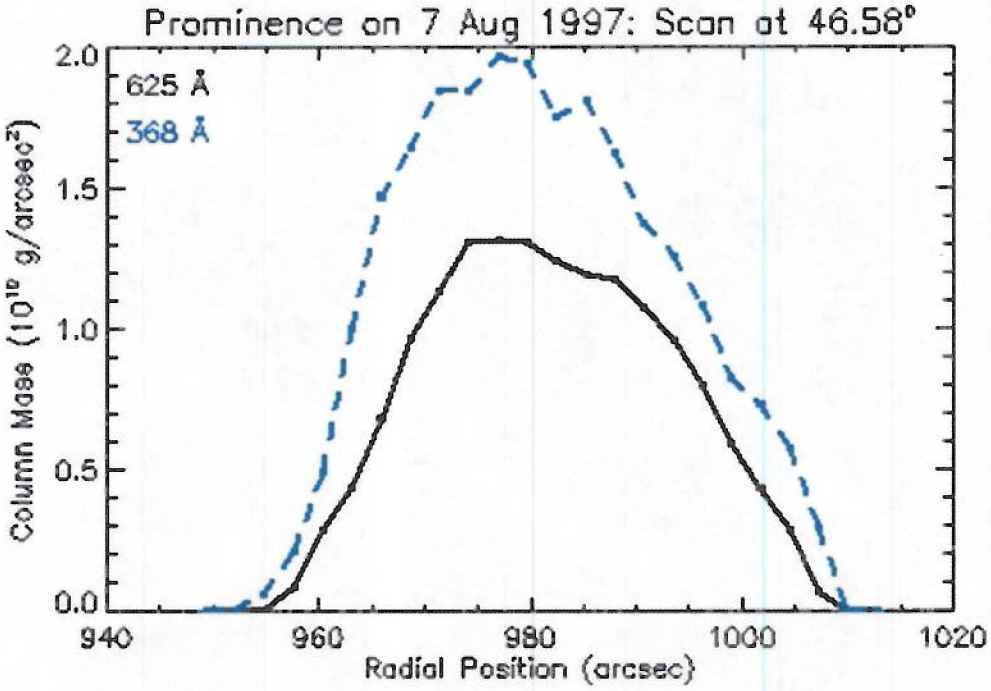
Prominence on 7 Aug 1997: Scan at 46.58°
625 Å
368 Å
Column Mass (10^{15} g/arcsec^2)
2.0
1.5
1.0
0.5
0.0
940
960
980
1000
1020
Radial Position (arcsec)

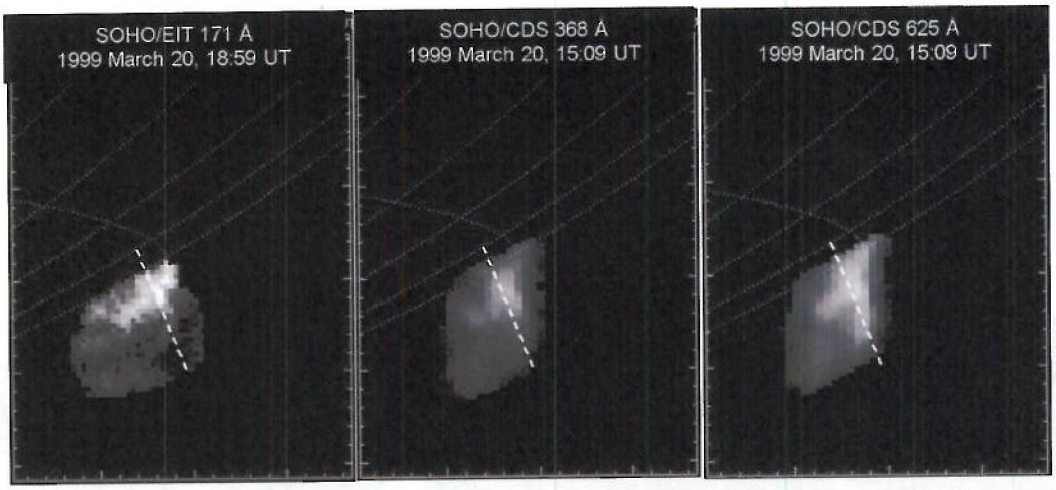
SOHO/EIT 171 Å
1999 March 20, 18:59 UT
SOHO/CDS 368 Å
1999 March 20, 15:09 UT
SOHO/CDS 625 Å
1999 March 20, 15:09 UT

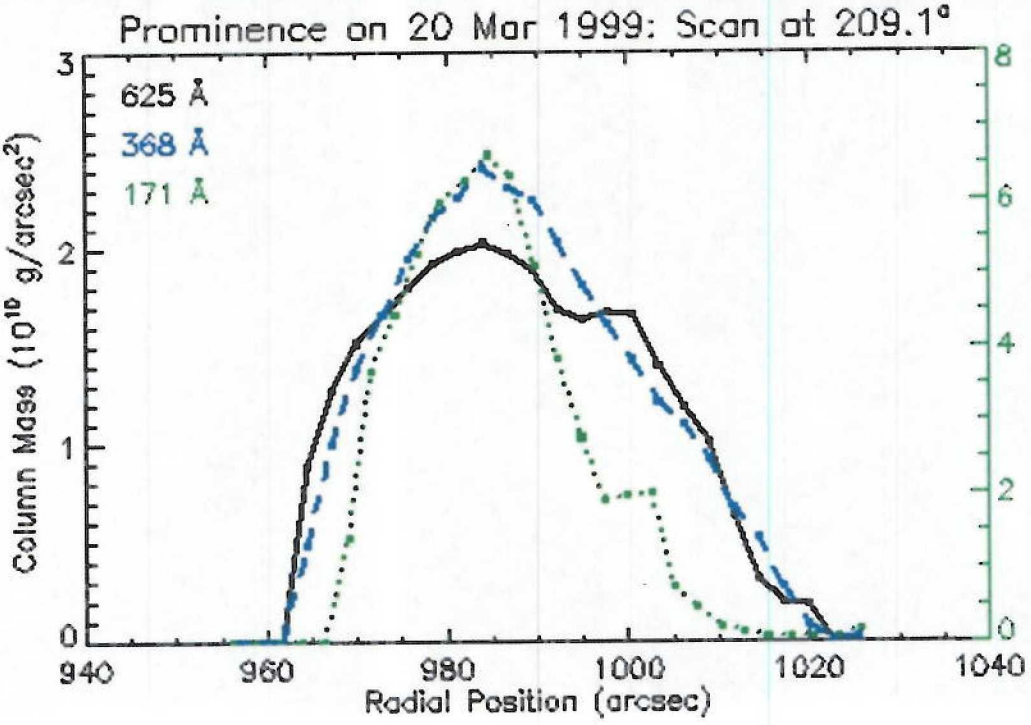
Prominence on 20 Mar 1999: Scan at 209.1°
625 Å
368 Å
171 Å
Column Mass (10^{18} g/arcsec^2)
Radial Position (arcsec)
0
1
2
3
940
960
980
1000
1020
1040
0
2
4
6
8

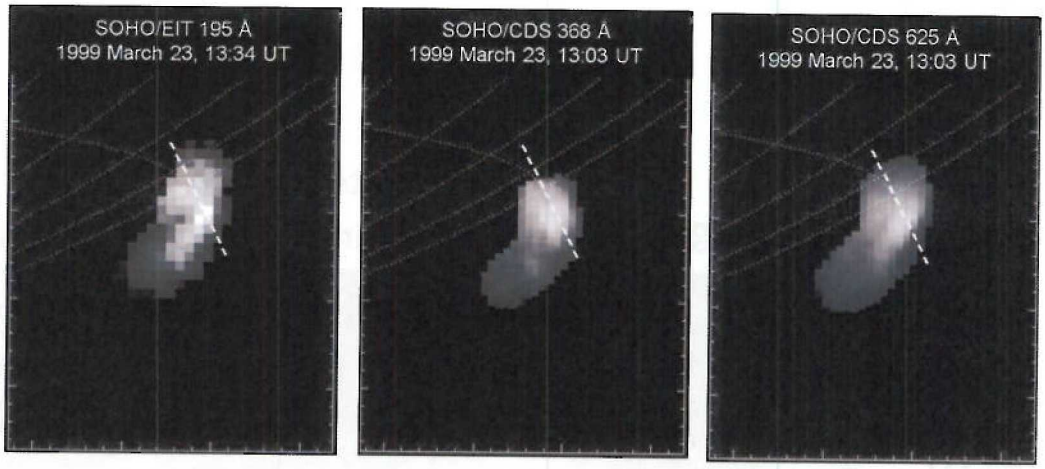
SOHO/EIT 195 Å
1999 March 23, 13:34 UT
SOHO/CDS 368 Å
1999 March 23, 13:03 UT
SOHO/CDS 625 Å
1999 March 23, 13:03 UT

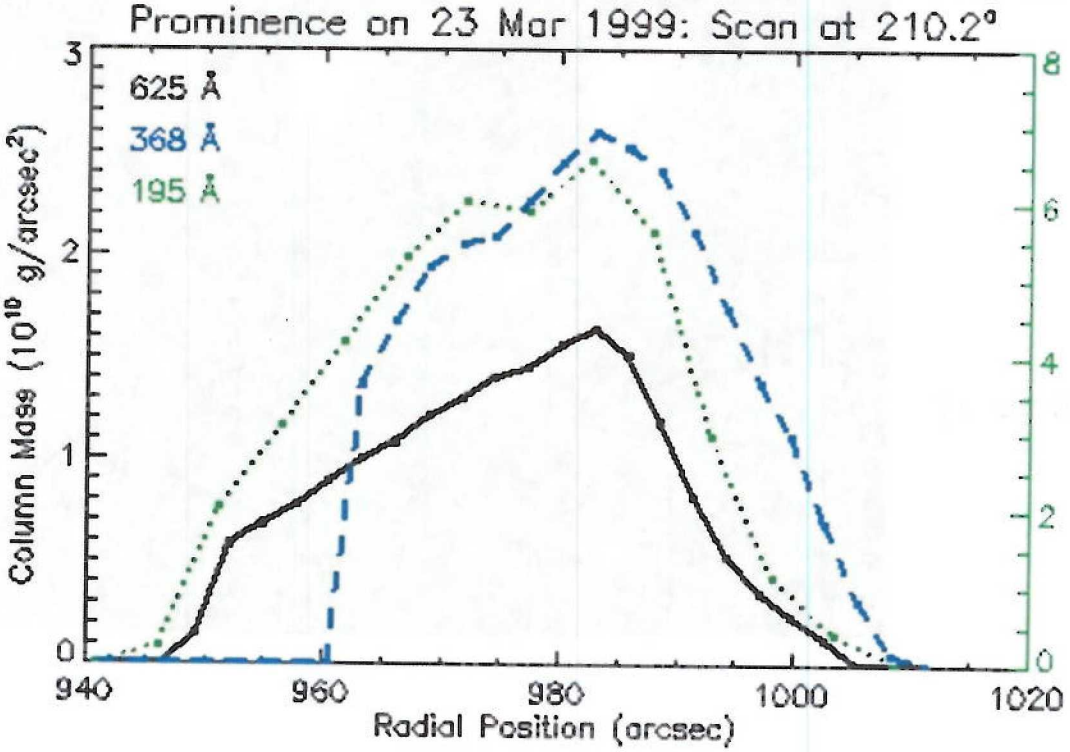
Prominence on 23 Mar 1999: Scan at 210.2°
625 Å
368 Å
195 Å
Column Mass (10^{19} g/arcsec^2)
Radial Position (arcsec)
0
1
2
3
4
6
8
940
960
980
1000
1020

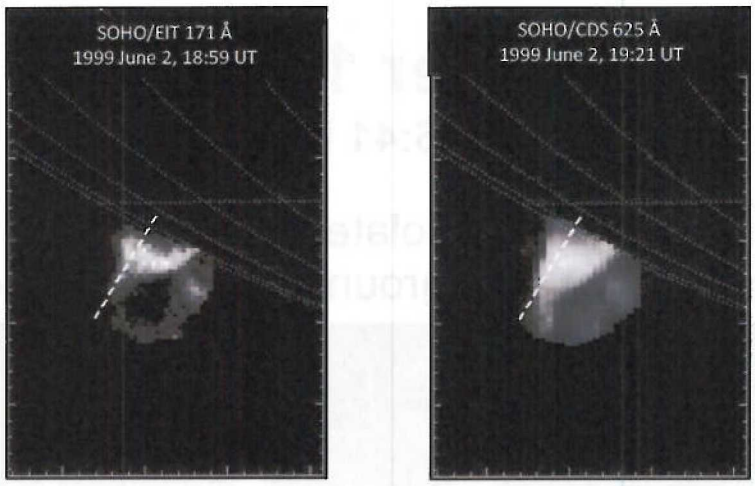
SOHO/EIT 171 Å
1999 June 2, 18:59 UT
SOHO/CDS 625 Å
1999 June 2, 19:21 UT

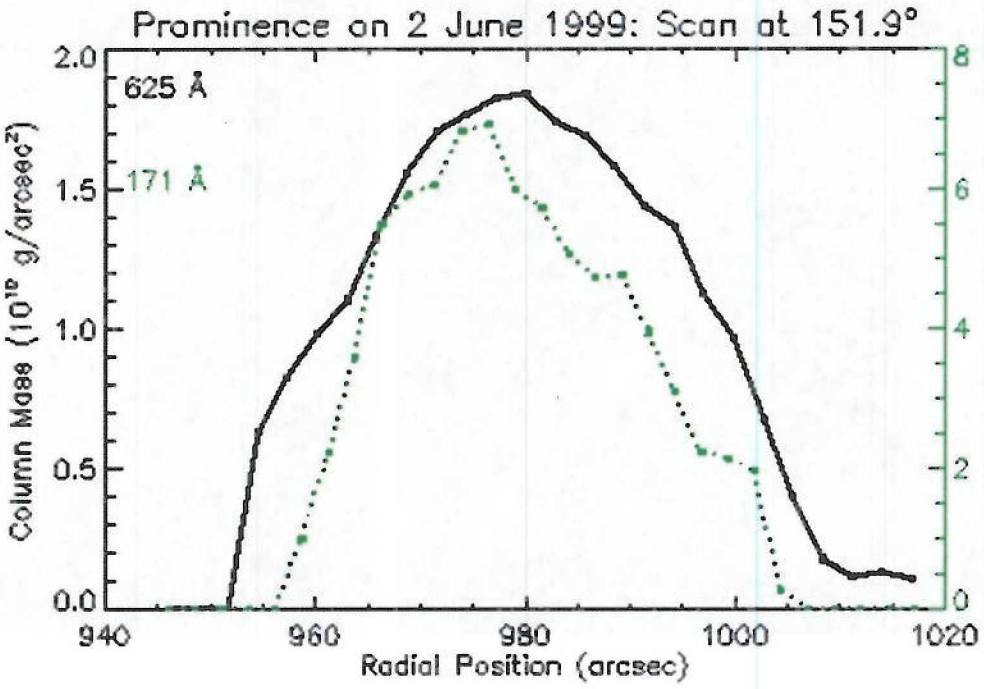
Prominence on 2 June 1999: Scan at 151.9°
625 Å
171 Å
Column Mass (10^{19} g/arcsec^2)
Radial Position (arcsec)
0.0
0.5
1.0
1.5
2.0
940
960
980
1000
1020
0
2
4
6
8


SOHO/CDS 625 A
1999 Oct. 12, 16:41 UT
SOHO/CDS 368 A
1999 Oct. 12, 16:41 UT
SOHO/EIT 171 A
1999 Oct. 12, 19:27 UT

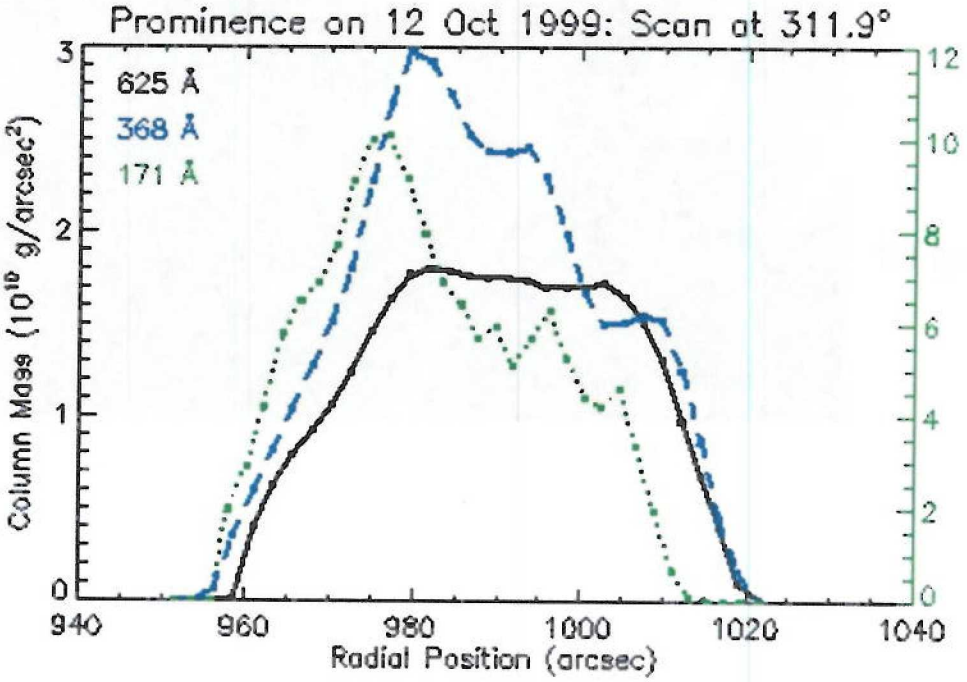
Prominence on 12 Oct 1999: Scan at 311.9°
625 Å
368 Å
171 Å
Column Mass (10^{19} g/arcsec^2)
Radial Position (arcsec)
0
1
2
3
0
2
4
6
8
10
12
940
960
980
1000
1020
1040

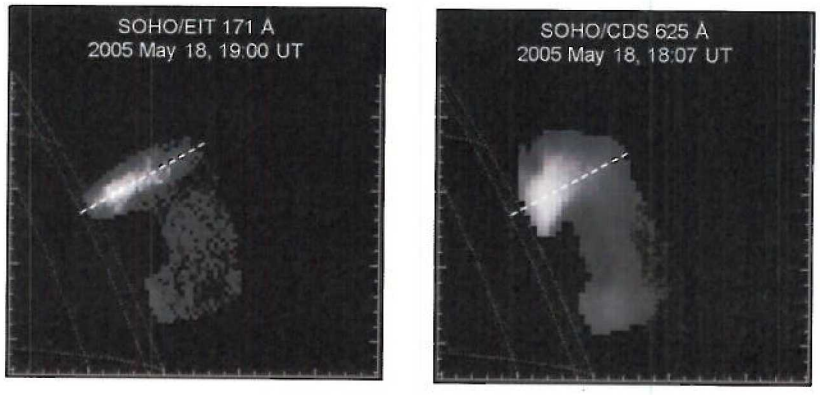
SOHO/EIT 171 Å
2005 May 18, 19:00 UT
SOHO/CDS 625 Å
2005 May 18, 18:07 UT

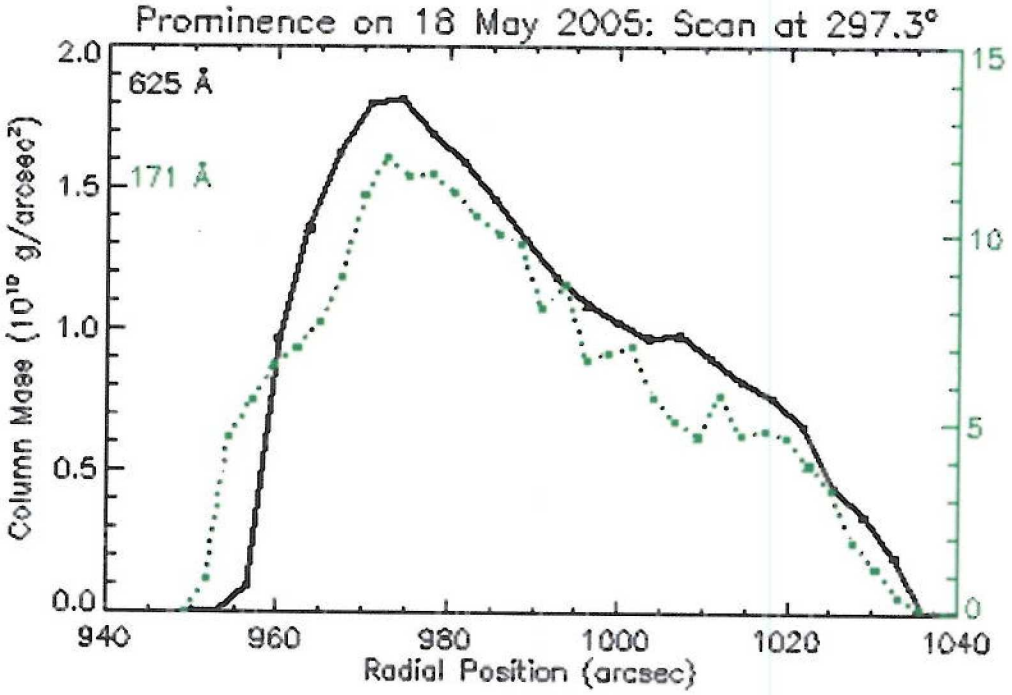
Prominence on 18 May 2005: Scan at 297.3°
625 Å
171 Å
Column Mass (10^19 g/arcsec^2)
Radial Position (arcsec)
2.0
1.5
1.0
0.5
0.0
15
10
5
0
940
960
980
1000
1020
1040